Geophysical Journal International

Geophys. J. Int. (2024) **237,** 1235–1248
Advance Access publication 2024 March 21
GJI Seismology

https://doi.org/10.1093/gji/ggae115

Incorporating topographic effects in surface wave tomography based on shortest-path ray tracing

Nanqiao Du,[1] Tingwei Yang,[2,3] Tao Xu[3,4] and Qinya Liu[1,5]

[1] *Department of Earth Science, University of Toronto, Toronto, ON, M5S3B1, Canada. E-mail: nanqiao.du@mail.utoronto.ca*
[2] *College of Earth and Planetary Sciences, University of Chinese Academy of Sciences, Beijing,* 100049*, China*
[3] *Key Laboratory of Mineral Resources, Institute of Geology and Geophysics, Chinese Academy of Sciences, Beijing,* 100029*, China*
[4] *Innovation Academy for Earth Science, Chinese Academy of Sciences, Beijing,* 100029*, China*
[5] *Department of Physics, University of Toronto, Toronto, ON, M5S1A7, Canada*

Accepted 2024 March 20. Received 2024 March 3; in original form 2023 July 22

SUMMARY

We propose a new method to obtain 3-D shear wave velocity structures for regions with undulating topography based on surface wave dispersion data. In our method, we assume that surface waves propagate along a curved free surface, and the dispersion effects of these waves can be modelled as a frequency-dependent ray tracing problem. We use the shortest-path method to address off-great-circle propagation arising from inhomogeneous elastic parameters and topographic variations. We then apply our method to both synthetic and real-data inversions and demonstrate that ignoring topographic effects may significantly distort the inverted images. Finally, we analysed the accuracy of our method and provided a rule-of-thumb principle to quantitatively assess the need to account for topographic effects in surface wave tomography for a region.

Key words: Inverse theory; Seismic tomography; Surface waves and free oscillations; Wave propagation.

1 INTRODUCTION

Mapping variations of subsurface elastic parameters is crucial for the comprehensive understanding of dynamic processes in the shallow and deep Earth. Surface wave tomography provides a powerful tool for imaging these variations, particularly thanks to the growing availability of surface wave data from ambient-noise signals recorded by dense seismic arrays (Shapiro *et al.* 2005). Successful applications of surface wave tomography have been performed at different scales, including regional (e.g. Schmandt & Clayton 2013; Chen *et al.* 2016; Wang *et al.* 2019, 2020), continental (e.g. Yang *et al.* 2007; Saygin & Kennett 2012; Shen *et al.* 2016) and global (e.g. Schaeffer & Lebedev 2013; Chang *et al.* 2015) scales.

Surface waves are generally dispersive whereby traveltimes are frequency-dependent. This property enables the modelling of surface wave traveltime as a frequency-dependent ray tracing problem along the 2-D free surface of the Earth. Surface wave tomography methods often differ based on the methods used to calculate surface wave traveltime, including the great-circle surface wave tomography (Yang *et al.* 2007; Shen *et al.* 2018), eikonal tomography (Rawlinson *et al.* 2008; Arroucau *et al.* 2010) and finite-frequency tomography (Lin & Ritzwoller 2010; Guo *et al.* 2018). However, for regions with considerable topographic variations, these methods often neglect the effects of topography by assuming that the scale of topography is significantly smaller compared to the wavelength and penetration depth of surface waves (Wang & Sun 2019), which may be valid in most applications. For example, by using the spectral element method, Köhler *et al.* (2012) demonstrated that a 2-km variation of topography along a 200-km profile would only result in a 0.7 per cent underestimation of phase velocities at a 3-s period.

However, with the emergence of short-period nodal arrays and distributed acoustic sensors, the wavelength of short-period surface waves may become comparable to the scale of topography (Wang & Sun 2019). In addition, for regions with the substantial topographic variation (such as array profiles across Tibetan Plateau, onshore/offshore, etc.), the topographic effect cannot be overlooked even for surface waves recorded by broad-band seismometers (Jin *et al.* 2023). In such cases, it is imperative to consider the effect of topography in the forward modelling of surface wave traveltime or data processing. Koulakov *et al.* (2016) pioneered the inclusion of topography into surface wave ray tracing using a modified version of the pseudo-bending method (Um & Thurber 1987). Wang & Sun (2019) subsequently applied this method to short-period data to examine the impact of topography on inversion and identified potential bias when topography is not considered. Miller (2022) implemented the finite-difference method (Vidale 1988) to solve the modified eikonal equation for undulating topography. This methodology aligns with the work of Hibert *et al.* (2014), which applied a

similar approach to compute distances on topographic surfaces, akin to ray tracing, under the assumption of constant velocity. Alternatively, topographic effects can be removed from post-processing, as demonstrated by Jin *et al.* (2023) who employed numerical methods to quantitatively fit the linear relationship between anomaly shifts and topographic variations.

In this paper, we proposed the shortest-path method (SPM) for surface wave ray tracing by incorporating topographic effects. The paper is structured as follows: we begin by introducing the SPM, which aims to incorporate topographic effects in surface wave propagation. Next, we conduct a series of synthetic tests to demonstrate the advantages of our new method for regions with substantial topography. We then apply our method to real seismic data sets recorded over a polymetallic ore field to evaluate its effectiveness. Finally, we discuss the accuracy of our method and discuss the scenarios and applications in which topographical effects can be safely ignored.

2 METHOD

2.1 Surface wave WKBJ theory

In the surface wave WKBJ (Wentzel–Kramers–Brillouin–Jeffreys) theory, the slow variation assumption is usually adopted where surface waves propagate along the curved surface with rapidly varying phase terms and slowly varying amplitude (Woodhouse 1974; Tromp 1994). Therefore, we can take the ansatz that

$$u(\epsilon x^\alpha, z, \epsilon t) = A(\epsilon x^\alpha, z, \epsilon t)\mathrm{e}^{-i\frac{\Psi(\epsilon x^\alpha, \epsilon t)}{\epsilon}}, \tag{1}$$

where x^α ($\alpha = 1, 2$) are the contravariant coordinates on the free surface with possible undulating topography and ϵ is a small parameter. We can then define the local instant frequency ω and the wavenumber vector $\boldsymbol{k}$ based on the phase term Ψ as

$$\begin{aligned} k_\alpha &= \epsilon^{-1}\frac{\partial \Psi}{\partial x^\alpha}, \\ \omega &= -\epsilon^{-1}\frac{\partial \Psi}{\partial t}, \end{aligned} \tag{2}$$

where k_α is the covariant component of the wavenumber vector. Substituting the above equations into the wave equation and keeping only the zeroth-order term, we can determine the local dispersion relation $\omega = \Omega(k_\alpha, x^\alpha)$ and the corresponding Hamilton–Jacobi equation (Woodhouse & Wong 1986)

$$\frac{\partial \Psi}{\partial t} + \Omega(k_\alpha, x^\alpha) = 0. \tag{3}$$

For our study, we focus on the isotropic case where the local dispersion relation becomes $\omega = \Omega(k, x^\alpha)$ (k is the magnitude of $\boldsymbol{k}$). By employing the method of characteristics, the canonical equations for surface waves become

$$\begin{aligned} \dot{x}^\alpha &= \left(\frac{\partial \Omega}{\partial k_\alpha}\right) = \left(\frac{\partial \Omega}{\partial k}\right)\left(\frac{\partial k}{\partial k_\alpha}\right) = Uk^\alpha/k, \\ \dot{k}_\alpha &= -\left(\frac{\partial \Omega}{\partial x^\alpha}\right)_{\boldsymbol{k}} = \left(\frac{\partial \Omega}{\partial k}\right)_{\boldsymbol{x}}\left(\frac{\partial k}{\partial x^\alpha}\right)_{\Omega} = -\frac{\omega U}{c^2}\left(\frac{\partial c}{\partial x^\alpha}\right)_k, \\ \dot{\omega} &= 0, \end{aligned} \tag{4}$$

where $c = \Omega/k$ is the phase velocity, $U = \partial\Omega/\partial k$ is the group velocity and $\dot{x} = \mathrm{d}x/\mathrm{d}t$. Note that we can define the arclength on the surface as

$$\mathrm{d}s = \sqrt{g_{\alpha\beta}\mathrm{d}x^\alpha \mathrm{d}x^\beta} = \mathrm{d}t\frac{U}{k}\sqrt{g_{\alpha\beta}k^\alpha k^\beta} = U\mathrm{d}t, \tag{5}$$

where $g_{\alpha\beta}$ is the metric tensor on the free surface. By inserting eq. (5) into eq. (4), we can obtain

$$\begin{aligned} \frac{\mathrm{d}x^\alpha}{\mathrm{d}s} &= \frac{k^\alpha}{k}, \\ \frac{\mathrm{d}k_\alpha}{\mathrm{d}s} &= -\frac{\omega}{c^2}\left(\frac{\partial c}{\partial x^\alpha}\right)_k, \\ \frac{\mathrm{d}\omega}{\mathrm{d}s} &= 0. \end{aligned} \tag{6}$$

From eq. (6), we can make two key observations: First, ω is constant along the ray path. Secondly, for isotropic case, the surface wave ray path is solely determined by the phase velocity (Yomogida & Aki 1985). Another equivalent form of these equations is the Lagrangian of the system and the corresponding variational principle as

$$L = k_\alpha \dot{x^\alpha} - \Omega, \quad \delta\int_{\mathrm{A}}^{\mathrm{B}} L\,\mathrm{d}s = 0, \tag{7}$$

where A and B are two points located on the free surface. As ω is constant on the ray path, by defining the phase traveltime as $\mathrm{d}t(\omega) = \mathrm{d}s/c(\omega)$, we can derive Fermat's principle as

$$\delta t(\omega) = \delta\int_{\mathrm{A}}^{\mathrm{B}} \frac{\mathrm{d}s}{c(\omega)} = 0. \tag{8}$$

For first arrivals, the traveltime is usually obtained as minimum traveltime for all paths connecting A and B. When the phase velocity remains constant for a given frequency, the minimum traveltime for first arrivals is equivalent to finding the shortest path that connects points A and B on the free surface. This serves as the fundamental basis for the SPM method.

2.2 The shortest-path method for surface wave ray tracing

The SPM is a type of ray tracing method based on graph theory, which was first introduced by Moser (1991) for seismic ray tracing. Since then, efforts have been made to enhance its accuracy, flexibility and computational efficiency (Cao & Greenhalgh 1993; Zhou & Greenhalgh 2005; Bai *et al.* 2007, 2010; Li *et al.* 2020). Unlike finite-difference based methods such as Fast Marching Method (Sethian & Popovici 1999) and Fast Sweeping Method (Zhao 2005), SPM provides a more adaptable framework for challenging ray tracing problems, as it allows for the incorporation of irregular surfaces or discontinuities with relative ease (Zhou & Greenhalgh 2005). In this study, our aim is to extend the SPM to surface wave ray tracing with topography. The primary steps involved in the forward modelling of SPM can be summarized in the next section, as also noted in Bai *et al.* (2007) and Li *et al.* (2020).

2.2.1 Model discretization and traveltime initialization

In the SPM method, the 2-D (curved) free surface is discretized by quadrilateral elements to accommodate variations of topography, as shown in Fig. 1. The nodes located at the corners of each element are referred to as *primary nodes* (black dots in Fig. 1) that serve to represent the location and shape of each element. To accurately determine the position of each ray segment, a set of *auxiliary nodes* are evenly added to the edges of each element, with the total number of nodes on each edge along the two coordinate directions denoted by $N_x^{(1)}$ and $N_y^{(1)}$, respectively (see Fig. 1, right panel), and the density of nodes can be adjusted based on the specific applications. The velocities at both types of nodes are interpolated from external models through bilinear interpolation. The combination of primary

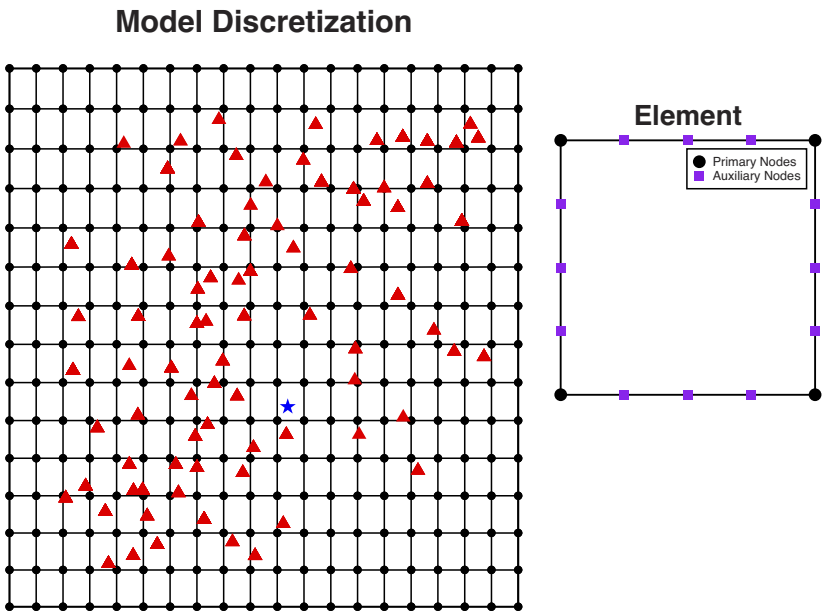

Figure 1. The meshing of a velocity model in SPM. Left panel: The study area is divided into $N_x \times N_y$ regular quadrilateral elements. The black dots are the primary nodes where velocity is assigned. The blue asterisk is the location of the event, and red triangles are the locations of all stations. Right panel: The purple squares (three nodes on each side for this case) are auxiliary nodes used to help determine the minimum traveltime and locate the ray path.

and auxiliary nodes can help increase ray coverage in each element and avoid using a large number of total elements (Zhou & Greenhalgh 2005). It is worth noting that although a structured quadrilateral mesh is used in this study, other options such as triangular or unstructured quadrilateral meshes can be also used in combination with primary–auxiliary nodes. The nodes in the discretization, both primary and auxiliary, are identified by a global numbering system $\{\boldsymbol{x}_n\}$, $n = 1, \cdots, N$, where N is the total number of global nodes. The continued calculation of traveltime across edges of adjacent elements allows for the representation of frequency-dependent traveltime at each node, denoted by $\{t_n(\omega)\}$.

In the SPM, nodes are assigned one of three labels: '*unfinished*' (not yet visited), '*activated*' (visited and value tentatively assigned) and '*finished*' (visited and value permanently assigned). For the initiation of the ray tracing procedure for a specific event, the event location $\boldsymbol{x}_s$ is first assigned a zero traveltime, while all nodes are assigned infinity traveltime and labelled as '*far*'. Both 'far' and 'activated' nodes are considered 'unfinished'. Next, the traveltime at the ith node on the edges of the source element Ω_s can be calculated as

$$t_i(\omega) = \frac{|\boldsymbol{x}_i - \boldsymbol{x}_s|}{2}\left[\frac{1}{c(\omega, \boldsymbol{x}_i)} + \frac{1}{c(\omega, \boldsymbol{x}_s)}\right], \tag{9}$$

where $|\cdot|$ is the geodesic distance on the free surface (approximated by straight line in this study) and $c(\omega, \boldsymbol{x}_i)$ is the phase velocity at the ith node. Finally, we alter the label of all these nodes to 'activated'.

2.2.2 *Compute frontal traveltimes*

In this step, we utilize Dijkstra's algorithm (Moser 1991) to systematically advance our wave front by assigning the 'finished' label to the existing set of 'activated' nodes. Specifically, we first select the node $\boldsymbol{x}_j$ with minimum traveltime among the set of 'activated' nodes, and then set the label of this node to 'finished'. We then assign the 'activated' label to all unfinished neighbouring nodes that share an element with node $\boldsymbol{x}_j$. The traveltimes on these nodes are updated via the application of the trapezoid rule and Fermat's principle as

$$t_i(\omega) = \min\left\{t_i(\omega), t_j(\omega) + \frac{|\boldsymbol{x}_i - \boldsymbol{x}_j|}{2}\left[\frac{1}{c(\omega, \boldsymbol{x}_i)} + \frac{1}{c(\omega, \boldsymbol{x}_j)}\right]\right\}, \tag{10}$$

using similar notation as eq. (9). If a station resides in an element Ω_r with all nodes labelled 'finished', we then update its traveltime using

$$t(\boldsymbol{x}_r) = \min_{\forall \boldsymbol{x}_j \in \Omega_r}\left\{t_j(\omega) + \frac{|\boldsymbol{x}_r - \boldsymbol{x}_j|}{2}\left[\frac{1}{c(\omega, \boldsymbol{x}_i)} + \frac{1}{c(\omega, \boldsymbol{x}_j)}\right]\right\}. \tag{11}$$

And this step should be iteratively repeated until the traveltimes of all stations are updated.

2.2.3 *Ray tracing*

The SPM presents an elegant approach to obtain the exact ray trajectory while simultaneously updating traveltimes on all nodes. As presented in eq. (10), it is evident that when updating the traveltime on a node i via node j, the wave front must have travelled from incident node j to objective node i. Hence, the ray coordinates can be determined by preserving the relevant incident node at each step during traveltime update. Subsequently, one can trace the sequence of incident nodes from each station to event source location to obtain the ray paths.

The ray tracing methodology presented above is applicable exclusively to traveltimes associated with phase velocity. As shown by eq. (6), the trajectory of a surface wave ray is solely determined by phase velocity. To compute the traveltime of a wave packet, we should first determine the ray path based upon the corresponding phase velocity at the same period. Then, the traveltime can be calculated by setting $c(\omega)$ in eqs (9)–(11) velocity to group velocity $U(\omega)$.

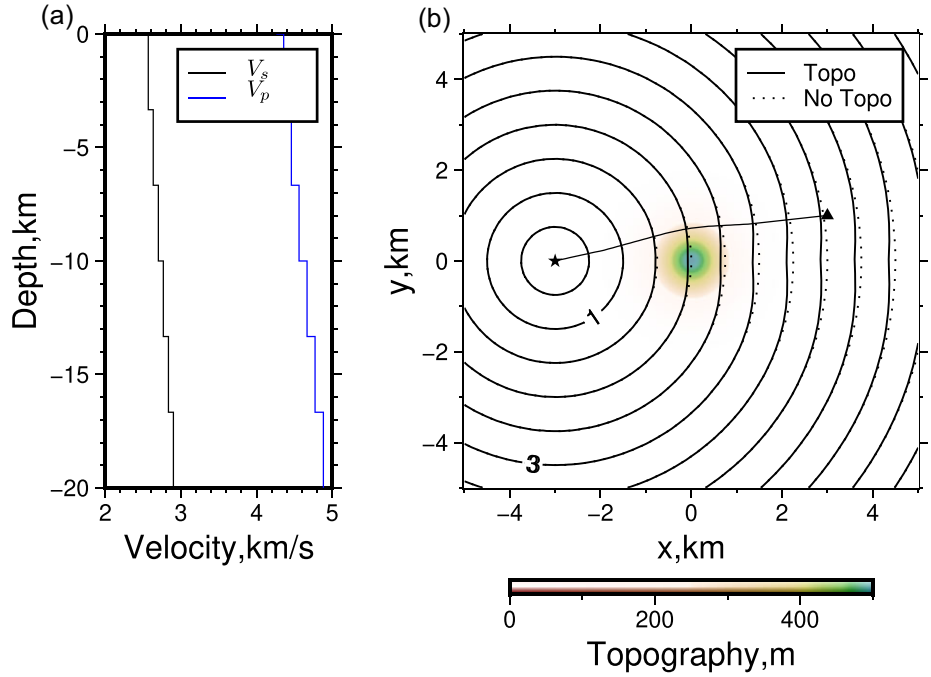

Figure 2. Traveltime field for a simple model with a Gaussian mountain. (a) Vp and Vs profiles for a simple 1-D model. The velocities at mountains are the same with other points off the mountain. (b) The computed traveltime field. The solid and dashed lines show the contours with and without topography, respectively. Black star and triangle are the source and station, respectively.

2.2.4 Advantages of SPM

The SPM approach offers several advantages compared with other surface wave ray tracing methods. First, the method is based on Fermat's principle (as described in eq. 10) and is readily implementable. The use of a heap sort algorithm during the updating step allows for efficient identification of the node with minimum traveltime, with the worst-case time complexity of $\Theta(E + n\log n)$ (n is the number of nodes and E is the number of edges for a graph). Secondly, SPM is flexible with respect to the choice of mesh structure, as it does not rely on a specific coordinate system. Therefore, a range of mesh configurations (e.g. triangular or quadrilateral mesh) can be utilized for different modelling scenarios. Thirdly, the accuracy of traveltime calculations can be improved by increasing the density of auxiliary nodes along the sides of each element (see more in Section 5). Moreover, the ray path between the source and any given node can be automatically determined once the traveltime has been updated. Finally, SPM allows for 'lazy computation', in which the simulation can be stopped once all traveltimes at the desired stations have been updated, without computing the full traveltime field.

2.3 The Fréchet kernel

The crucial step in inverting 2-D dispersion map involves computing the gradient of traveltime with respect to the current dispersion velocity. In order to obtain the discretized version of eq. (8), we make use of eqs (9) and (10) and rewrite eq. (8) as follows:

$$t_j(\omega) = \sum_{i=1}^{N} \frac{|\boldsymbol{x}_i - \boldsymbol{x}_j|}{2}\left(\frac{1}{c_i(\omega)} + \frac{1}{c_{i+1}(\omega)}\right). \tag{12}$$

Here, $\boldsymbol{x}_i$, $\boldsymbol{x}_{i+1}$ represent the two endpoints for segment i of the ray path from SPM, c_i and c_{i+1} are the phase/group velocities at each endpoint and t_j represents the jth traveltime at period ω. Based on the stationary properties of eq. (8), the first-order perturbation of the phase velocity results in second-order variation in the ray path, which is ignored in this study. As a result, the perturbation of the traveltime related to the perturbation of phase velocity along the ray can be expressed as:

$$\delta t_j(\omega) = -\sum_{i=1}^{N} \frac{|\boldsymbol{x}_i - \boldsymbol{x}_j|}{2}\left(\frac{\delta c_i}{c_i^2(\omega)} + \frac{\delta c_{i+1}}{c_{i+1}^2(\omega)}\right), \tag{13}$$

which suggests that the perturbation of all traveltimes can be related to perturbation of the ray velocity at all nodes in a matrix form:

$$\boldsymbol{\delta t}(\omega) = \boldsymbol{K}(\omega)\boldsymbol{\delta c}(\omega), \tag{14}$$

where matrix $\boldsymbol{K}(\omega)$ is the Fréchet kernel for a given frequency ω. Since the traveltime is only related to nodes near the ray path, the matrix $\boldsymbol{K}(\omega)$ will be quite sparse.

2.4 3-D direct inversion

For most surface wave tomography, eq. (14) gives the linear equations to invert from anomalies of dispersion curves to perturbations of 2-D dispersion maps at distinct frequencies ω (Barmin *et al.* 2001; Shen *et al.* 2016). In the 'two-step' surface wave tomography, the 3-D elastic model is usually considered as a stack of series of 1-D layered modes. Therefore, once the dispersion maps are determined for a series of frequencies, they can be combined to invert for local 1-D models beneath each point on the free surface. However, the intermediate step may introduce undesirable smoothing artefacts into the final results. Hence, in this study, we adopt a direct inversion method (West *et al.* 2004; Nunn *et al.* 2014; Fang *et al.* 2015; Du *et al.* 2021). In this approach, the variation of 1-D phase/group velocity is linked to the perturbation of elastic parameters based on a variational formula (Gomberg & Masters 1988; Aki & Richards 2002) and Thomson–Haskell propagator matrix algorithm

(Schwab & Knopoff 1972):

$$\delta c(\omega) = \left(\delta\boldsymbol{\beta}\cdot\nabla_\beta + \delta\boldsymbol{\alpha}\cdot\nabla_\alpha + \delta\boldsymbol{\rho}\cdot\nabla_\rho\right) c(\omega). \tag{15}$$

As the phase/group velocity is more sensitive to variations in *S*-wave velocity than in *P*-wave velocity and density (Dahlen & Tromp 1998), it is common to invert for variations in *S*-wave velocity only, while mapping *P*-wave velocity and density using Brocher's relations (Brocher 2005):

$$\alpha = F_\alpha(\beta),\ \rho = F_\rho(\beta). \tag{16}$$

Then we can combine eqs (14)–(16) to obtain the 3-D Fréchet kernel as

$$\begin{aligned} &t_i^{\mathrm{obs}}(\omega) - t_i^{\mathrm{syn}}(\omega;\beta) \approx \delta t_i(\omega) \\ &= \sum_{k=1}^{N} \frac{\partial t_i^{\mathrm{syn}}(\omega,\beta)}{\partial c_k(\omega)} \frac{\mathrm{d}c_k(\omega)}{\mathrm{d}\beta_j}\delta\beta_j, \end{aligned} \tag{17}$$

where $\mathrm{d}/\mathrm{d}\beta_j$ is the full partial derivative for the shear wave velocity at the jth node. This formula can be reorganized into a matrix form:

$$\boldsymbol{G}\,\delta\boldsymbol{\beta} = \delta\boldsymbol{t}, \tag{18}$$

and solved by adding regularization terms:

$$\begin{bmatrix} \boldsymbol{G} \\ \gamma\boldsymbol{L} \\ \theta\boldsymbol{I} \end{bmatrix} \delta\boldsymbol{\beta} = \begin{bmatrix} \delta\boldsymbol{t} \\ \boldsymbol{0} \\ \boldsymbol{0} \end{bmatrix}, \tag{19}$$

where $\boldsymbol{L}$ and $\boldsymbol{I}$ are the second- and zeroth-order Tikhonov regularization terms with corresponding coefficients γ and θ, respectively. This linear system can be efficiently solved by LSQR method (Paige & Saunders 1982), after which the current model (model at nth iteration) can be updated as

$$\boldsymbol{\beta}^{(n+1)} = \boldsymbol{\beta}^{(n)} + \delta\boldsymbol{\beta}^{(n)}. \tag{20}$$

3 SYNTHETIC TEST

3.1 Traveltime field for a 1-D model

The first synthetic test uses a simple 1-D isotropic layered model (Fig. 2a) defined on a rectangular block with a dimension of 10 × 10 km in the horizontal direction and 20 km in depth. Topography in the shape of a Gaussian mountain with a maximum height of 0.5 km and a standard deviation of 0.5 km is placed around at the centre of the region (Fig. 2b). The elastic parameters over the mountain are the same as those on the flat free surface. Next, we compute the phase velocity at a period of 1 s and utilize SPM to synthesize the traveltime field. The phase velocity and the mesh used are shown in Fig. 3.

The traveltime field depicted in Fig. 2 shows that the traveltime with topography (solid lines) matches the theoretical traveltime without topography (dashed lines) when waves do not interact with the Gaussian mountain. However, when surface waves interact with the mountain, the traveltime is delayed and deviates from the concentric circles and the ray paths are diffracted around the obstacle (Fig. 4). The time field and the ray path over the Gaussian mountain seem to exhibit similar behaviour as those of a low-velocity zone without topography, and hence may interfere with the ability to resolve and interpret anomalies directly beneath the topography.

3.2 Checkerboard test

We further conduct a synthetic test to validate our method. The modelling region spans approximately 10 km × 10 km with maximum depth 12 km. It also includes a Gaussian mountain 1 km in height and 2 km in width and a distribution of 87 stations as shown in Fig. 5(a). The Rayleigh wave phase/group dispersion data used is spanning a period range from 0.2 to 7.4 s. A histogram of the available dispersion data are shown in Fig. 5(b).

A checkerboard model of alternating high and low anomalies with the size of 2 km × 2 km is added to a given initial 1-D model, extending down to a depth of 10 km (Fig. 6). The velocity within the mountainous region is same as that of the colocated horizontal point on the free surface. In order to examine the topographic effects, the mountain is positioned directly over a high-velocity anomaly pattern. We first use Thomson–Haskell algorithm and SPM to generate the surface wave traveltime as synthetic data, and then apply the 3-D direct inversion method to recover the checkerboard model from the initial 1-D model, shown as both horizontal (at depth of 1.2 km) and vertical cross-sections along the profile A–A′ in Figs 6 and 7, respectively. Note that by incorporating topography in the initial model and traveltime calculations, the checkerboard velocity patterns can be successfully recovered as shown in both horizontal and vertical slices (Figs 6b and 7b). On the other hand, when the effect of topography is not accounted for, the high-velocity anomaly patterns directly beneath the mountain is overtaken by the low-velocity anomaly artefacts from the topography, as illustrated in the horizontal slices (Fig. 6a). Similar features can be observed in the vertical cross-section where a 'crustal plume' appears to be present right beneath the location of the mountain (Fig. 7a). This phenomenon is consistent with our previous observations that the traveltime delay caused by topography can introduce an artificial low-velocity anomaly pattern beneath it if the topographic effects are not considered in the forward modelling.

4 REAL-DATA APPLICATIONS

Now we apply our new surface-ray tracing method on a real short-period seismic data set recorded for the Qingchengzi ore field, located in the Liaodong Peninsula of Northeast China. This region represents a Pb–Zn–Au–Ag polymetallic ore field, characterized by the presence of two major fault systems, namely the Jianshanzi Fault (JSZF) and the 101 Fault (101F), as depicted in Fig. 8. The primary gold ore deposits (represented by the yellow dots in Fig. 8) are mostly located along these two major fault systems and their subfaults (Zeng *et al.* 2019).

The study area spanning approximately 50 km × 30 km horizontally exhibits a maximum topography of about 0.5 km. Continuous waveform data from 334 short-period sensors were recorded from 2019 June 8 to July 10 (Fig. 8a). Following pre-processing, cross-correlation and stacking of the noise data, frequency–time analysis (AFTAN) was applied to extract the phase-velocity dispersion curves (Bensen *et al.* 2007) for fundamental-mode Rayleigh waves over the period range of 0.3–3.0 s, as reported in Xie *et al.* (2021). Fig. 8(b) shows the histogram of the dispersion data used at each period. To obtain a suitable 1-D initial model, the Neighbourhood Algorithm (Sambridge 1999) is employed to fit the average dispersion curve (see Supporting Information Section S2). During the 3-D direct surface wave inversion process, the damping factor, θ in eq. (19), is held constant at a relatively small value (0.01 in this study) to maintain the stability of the LSQR solver. Furthermore, the

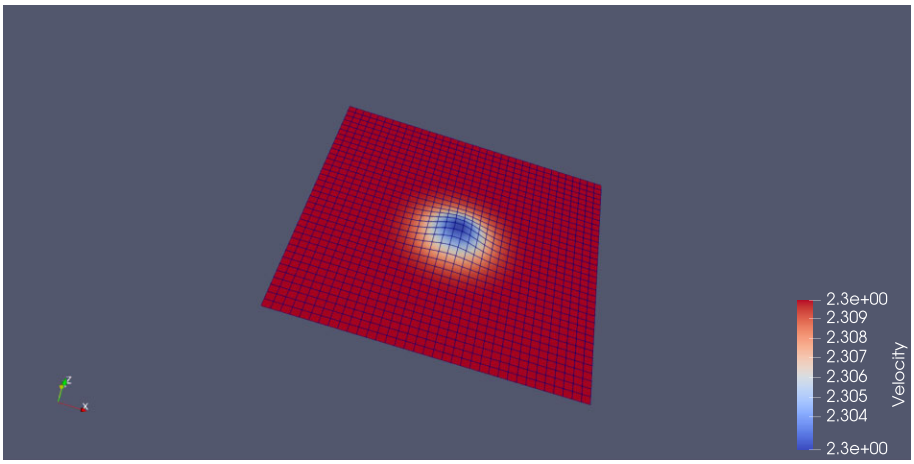

Figure 3. The topography-adaptive SPM mesh and the phase velocity distribution for 1-s period.

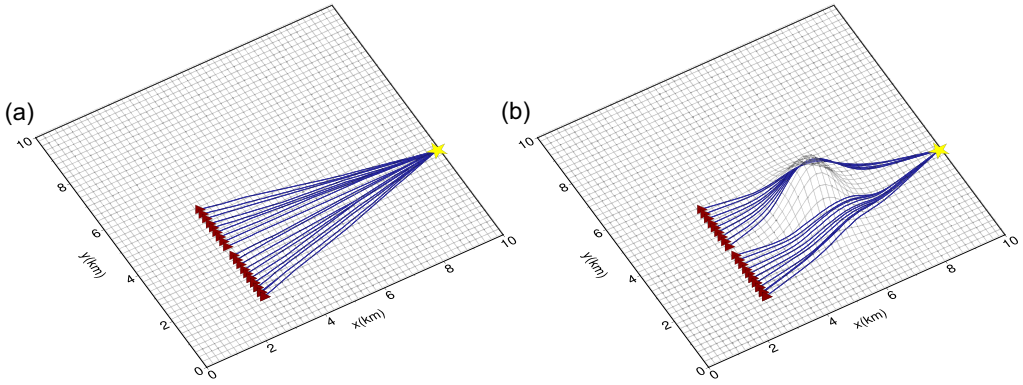

Figure 4. Ray paths for the Gaussian mountain model in Fig. 3: (a) without topography and (b) with topography.

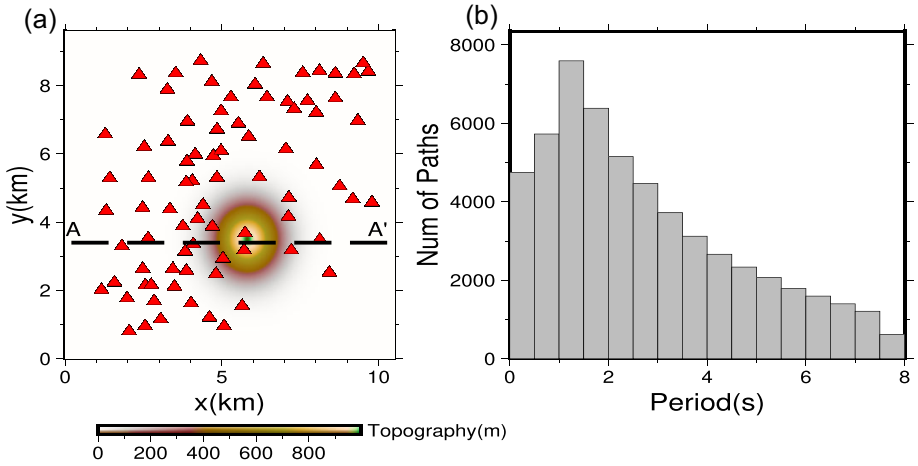

Figure 5. (a) The topography and station distribution for the checkerboard model. Red triangles are stations used. The dashed line with tag A–A′ is the profile we will use for showing the inversion results (Fig. 7b). The histogram for the number of dispersion data at each period.

smoothing factor, γ in eq. (19), is determined based on L-curve analysis (Aster *et al.* 2018), as detailed in the Supporting Information.

The final inversion results reveal the presence of a widely distributed low-velocity body (referred to as III in Fig. 9) within the central region of the Qingchengzi mining area, ranging from depths of 0.4 to 1.2 km. These low-velocity anomalies (III) are commonly interpreted as intrusions of low-velocity granite within the Paleoproterozoic Liaohe Formation (see Figs 9a–c). In contrast, the Baiyun gold belt (BYGB in Fig. 8) exhibits distinctive high-velocity characteristics within the marble limestone of the Dashiqiao Formation (Zeng *et al.* 2019), as observed in the high-velocity body (Ia) on the eastern side extending from shallow depths to approximately 1.2 km (Figs 9a–c). On the western side of the Baiyun gold belt, a separate high-velocity body (Ib) emerges at a depth of 2.0 km (Fig. 9d). Furthermore, a low-velocity intrusive anomaly (II) is observed at a depth of 2.0 km to the south of the gold belt, extending downward

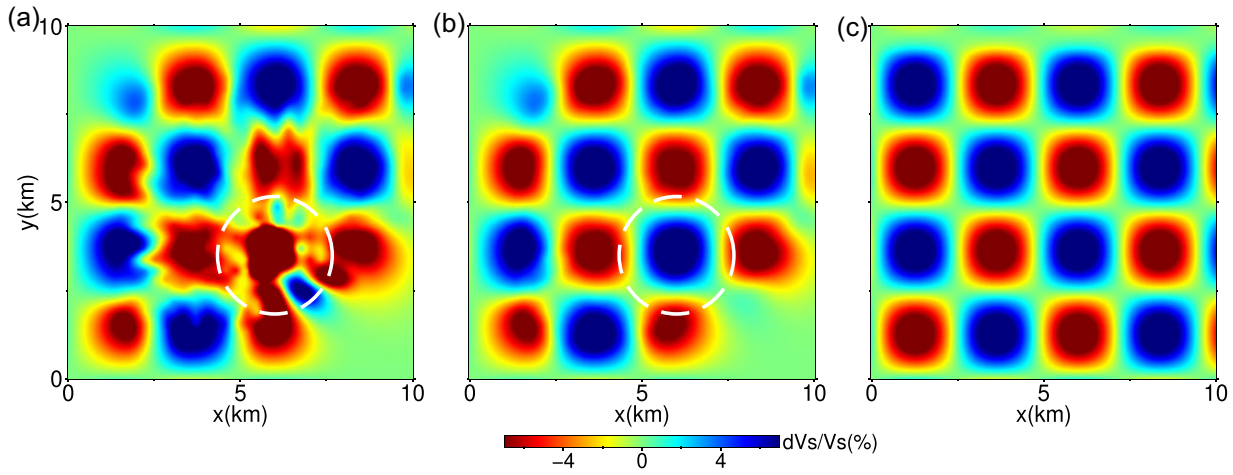

Figure 6. Horizontal slice at depth = 1.2 km. The white dotted line is the location of topography. (a) Inversion result without including topography. (b) Inversion result by including topography. (c) The true model.

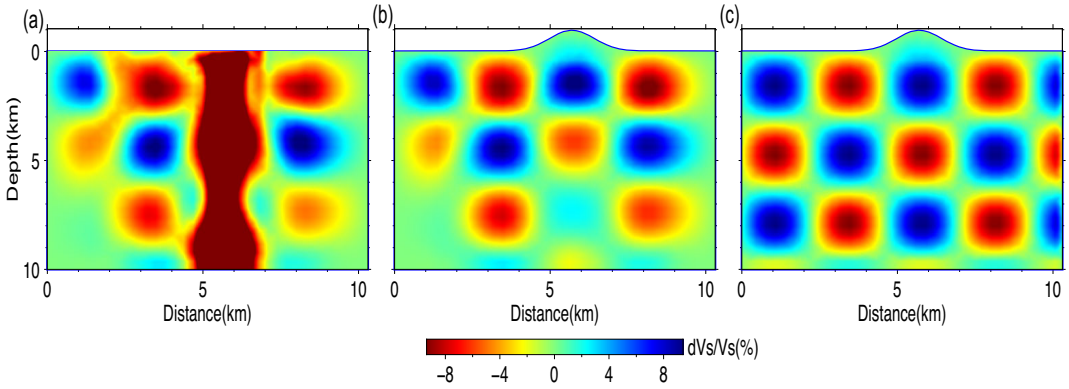

Figure 7. Inversion results across profile A–A′ across the synthetic Gaussian mountain. (a) Inversion result by using a flat model. (b) Inversion result by including topography. (c) The true model.

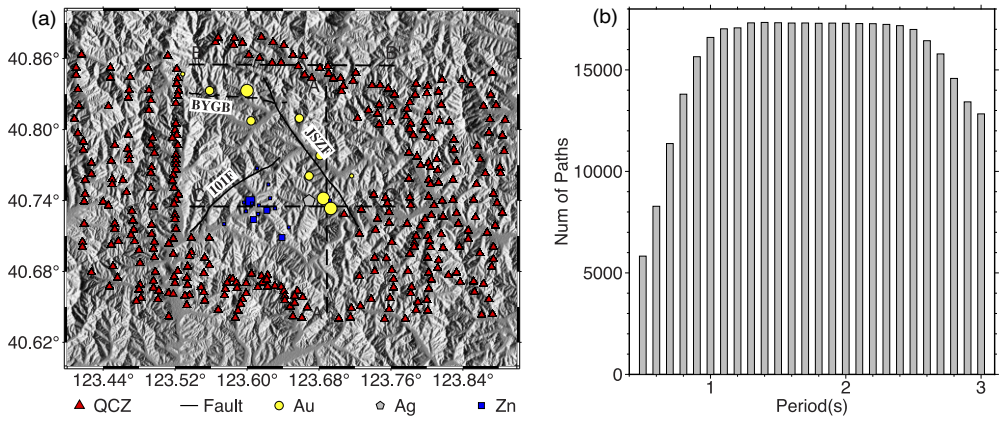

Figure 8. The Qingchengzi region and the data histogram. (a) The topography, fault system, ore deposits and station location in the study region. Profiles (dashed lines) A–C are used in Fig. 10 to show inversion results. The solid lines are the major fault systems in the region, and the dots with different colours are different types of ore deposits, with gold mines depicted by golden circles, silver mines by silver pentagons and Pb–Zn mines by blue squares. JSZF: Jianshanzi fault. 101F: 101 Fault. BYGB: Baiyun gold belt. (b) Histograms of Rayleigh wave phase dispersion data for each period.

from approximately 1.2 km (Figs 10a and b). These low-velocity anomalies may be attributed to gold mineralization associated with concealed granite intrusions which are typically accompanied by ore-forming fluids and low velocity (Figs 10a and b) as similarly interpretated by Xie *et al.* (2021).

While both inverted models (with and without including topography) have similar velocity patterns in general, several observations can be made by carefully comparing the two models. First, the model with topography shows a slightly better reduction in residuals (RMS = 0.157 s) than the model without topography

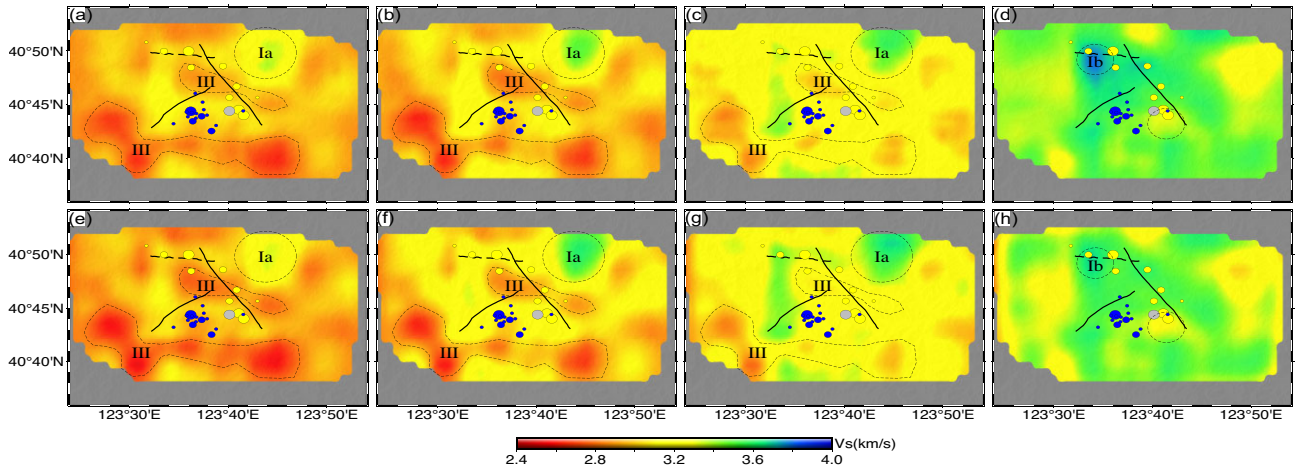

Figure 9. Horizontal slice at depth = 0.4, 0.8, 1.2, 2.0 km of the inverted model for Qingchengzi region shown from left to right by including topography (a–d) and without topography (e–h).

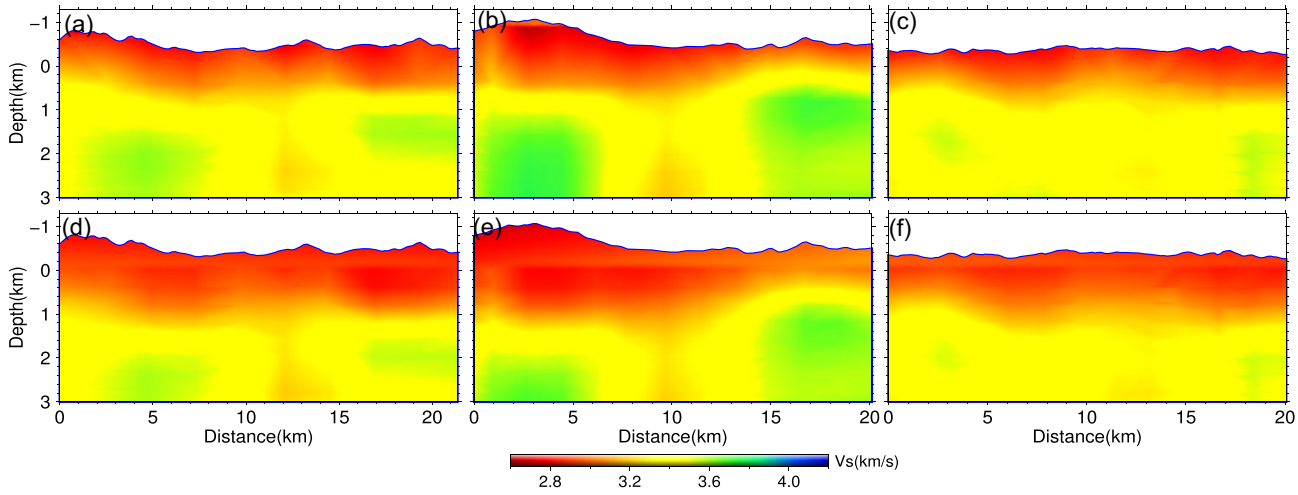

Figure 10. Vertical slices along profiles A–C in Figs 8. (a–c) Inversion result by including topography along profiles A–A′, B–B′ and C–C′ from left to right. (d–e) Inversion results without including topography along the same profiles.

(RMS = 0.161 s). At the depth of 1.2 km, the presence of the low-velocity anomaly (III) becomes more prominent in the model with topography (Fig. 9). Furthermore, in the same model, the high-velocity anomaly (Ib) located on the western side of the Baiyun gold belt (BYGB) at the depth of 2.0 km is stronger compared to the model without topography (Figs 9d and h).

5 DISCUSSION

5.1 Accuracy of SPM

One of the key characteristics of the SPM is its utilization of multiple straight-line segments to construct the ray path, connecting the source, nodes (both primary and auxiliary) and the receivers. Consequently, it is reasonable to hypothesize that the error would increase as the ray path derived from the SPM deviates further from the true ray path. To assess the accuracy of the method, it becomes essential to identify the specific region where the approximated paths potentially exhibit the greatest disparities compared to the true paths. To quantitatively analyse the error, we follow the approach of Bai *et al.* (2007) to define the relative traveltime error:

$$\delta = \frac{T - T_e}{T_e} = \frac{T}{T_e} - 1, \tag{21}$$

in which T_e is the true traveltime and T is the approximate traveltime from SPM. Gruber & Greenhalgh (1998) showed that for 2-D homogeneous media and square elements, the upper bound of the relative error is only dependent on the density of auxiliary nodes on each side of the cell as given by:

$$\delta_{ub} = \sqrt{2(n^2 + 1 - n\sqrt{n^2 + 1})} - 1 \approx \frac{1}{8n^2}, \tag{22}$$

where $n = M + 1$ and M is the number of auxiliary nodes on each side. Therefore, according to eq. (22), we know that simply increasing the number and decreasing the size of elements do not improve the computation accuracy in the homogeneous media (Gruber & Greenhalgh 1998).

By extending the previous accuracy analysis to heterogeneous media with complex velocity distributions or topographical variations, it is reasonable to hypothesize that the element size primarily contributes to enhancing the approximation of heterogeneity, and the auxiliary nodes are used to improve the computation accuracy

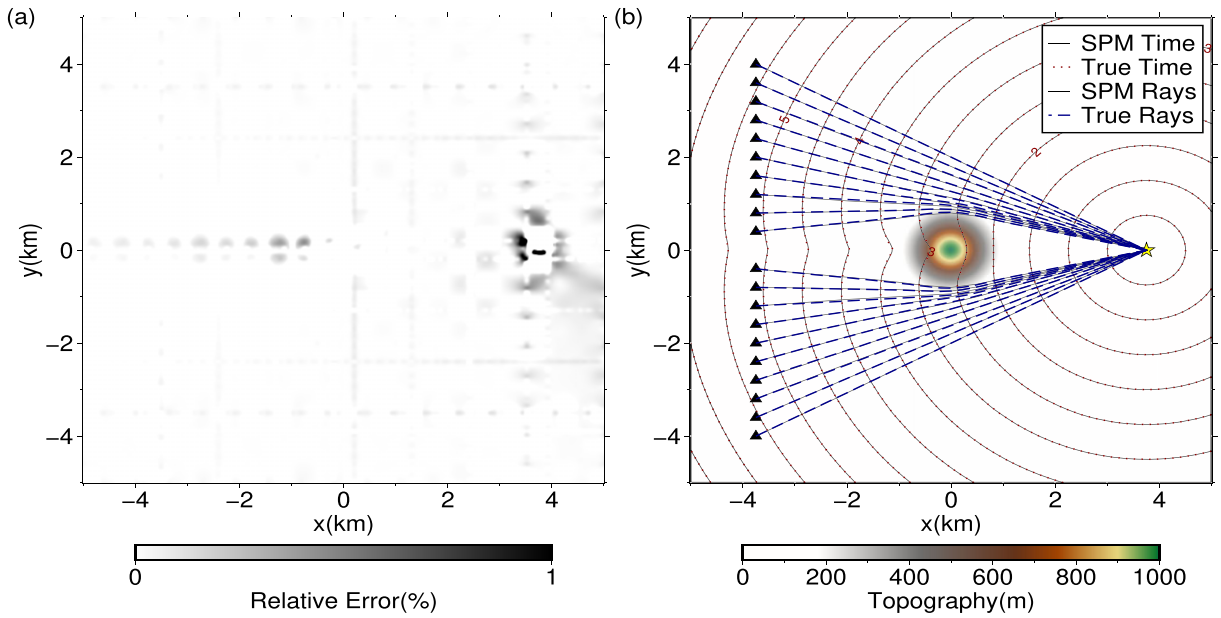

Figure 11. Traveltime field, time relative error and ray paths for model mesh with only 20 elements in each direction. There are 49 auxiliary nodes on each side of an element. (a) Relative error. (b) Traveltime field, topography and ray path comparison.

in well-sampled media. To validate this hypothesis, we perform a series of numerical experiments. In these experiments, we focus on a 10 km × 10 km region with homogeneous velocity at 1.5 km/s. The topography is a Gaussian mountain with a maximum height of 1.0 km and a standard deviation of 0.5 km placed around at the centre of the region, as shown in Fig. 11. For the 'ground-truth' traveltime, we use the traveltime path obtained from SPM applied to a very high-resolution model comprised of 200 × 200 elements with 49 auxiliary nodes along the edge of each element. We then gradually changed the size of elements and the density of auxiliary nodes to compute the relative traveltime error for each node based on eq. (21). Fig. 11(a) shows the relative traveltime error for each node while Fig. 11(b) shows the traveltime field in contours and the corresponding ray paths (solid lines) for a coarser model with merely 20 × 20 elements and 49 auxiliary nodes in each direction, compared to the 'ground-truth' traveltimes and ray paths. Remarkably, this coarser mesh with element size of 0.5 km is sufficient for adequately sampling the Gaussian mountain, and the ray paths closely resemble the true ray paths.

Fig. 12 presents the relative traveltime error for SPM mesh of 200 × 200 elements with varying numbers of auxiliary nodes (1, 5 and 11, respectively). In the case of a model with only one auxiliary node (Fig. 12a), notable discrepancies are observed in both the traveltime field and the ray paths. However, as the density of auxiliary nodes increases, the relative error gradually decreases, leading to ray paths that closely approximate the true paths (Fig. 12e). However, even with 11 auxiliary nodes, the 200 × 200-element model does not necessarily generate better traveltime results than the 20 × 20-element 49-auxiliary node model (Fig. 11). In addition, Fig. 13 shows the results for a mesh with 20 × 20 element and 11 auxiliary nodes which give similar relative errors as those of the 200 × 200 element 11-auxiliary node case (Figs 12e and f), but slightly worse errors than the 20 × 20 element 49-auxiliary node case (e.g. ray paths in Fig. 11 are slightly off the true paths in Fig. 13).

These experiments suggest that the effect of element size is to sufficiently sample the heterogeneity/topography in the study area, and the computational accuracy can be improved mainly by increasing the density of auxiliary nodes. However, it should be noted that employing a greater number of auxiliary nodes requires additional computational resources (the worst-case time complexity is $\Theta(E + n \log n)$). In practical applications, it is often recommended to have enough elements to sufficiently sample the complexities present in the study region, and employ 9–13 auxiliary nodes to strike a balance between accuracy and computational efficiency.

Another practical concern is the application of SPM in spherical coordinates. In our computation, we compute the distance between two points based on straight-line distance that deviates from the great-circle distance due to the Earth's curvature. While more precise small-distance approximations exist in spherical coordinates (Richter 1943), our straight-line approximation results in less than 1 per cent relative error for great-circle distance less than 5° in the spherical coordinate system. One possible solution is to sample the curvature with more elements in each direction for the forward SPM calculation. However, to reduce the computational cost, the original inversion mesh can still be used.

5.2 Is it possible to ignore topography?

From the checkerboard test shown in Section 3.2, it is clear that artefacts will be introduced to the final imaging results if surface topography is ignored in the forward modelling. To understand the impact of ignoring the topographic effect in surface wave tomography, we quantitatively analyse the error introduced by topography by examining the error propagation based on a linearized approach. We assume that the phase/group velocity is constant throughout the entire region and that the traveltimes for model with and without topography are t_{topo} and t, respectively. The time difference between

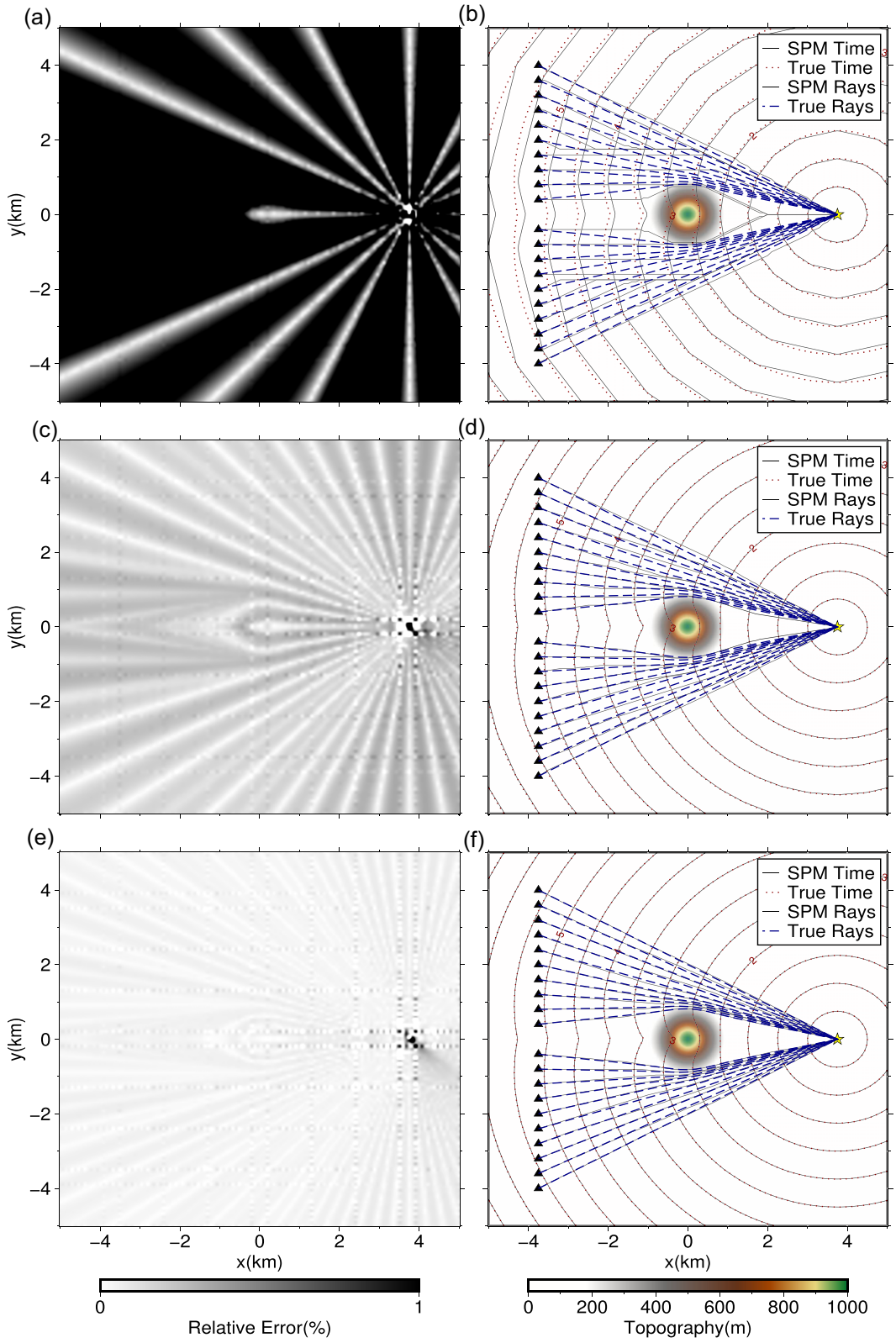

Figure 12. Same as Fig. 11, but the model mesh comprises 200 elements in each direction, with 1, 5 and 11 auxiliary nodes on each side of an element, respectively. (a and b) Results for one auxiliary node. (c an d) Results for five auxiliary nodes. (e and f) Results for 11 auxiliary nodes.

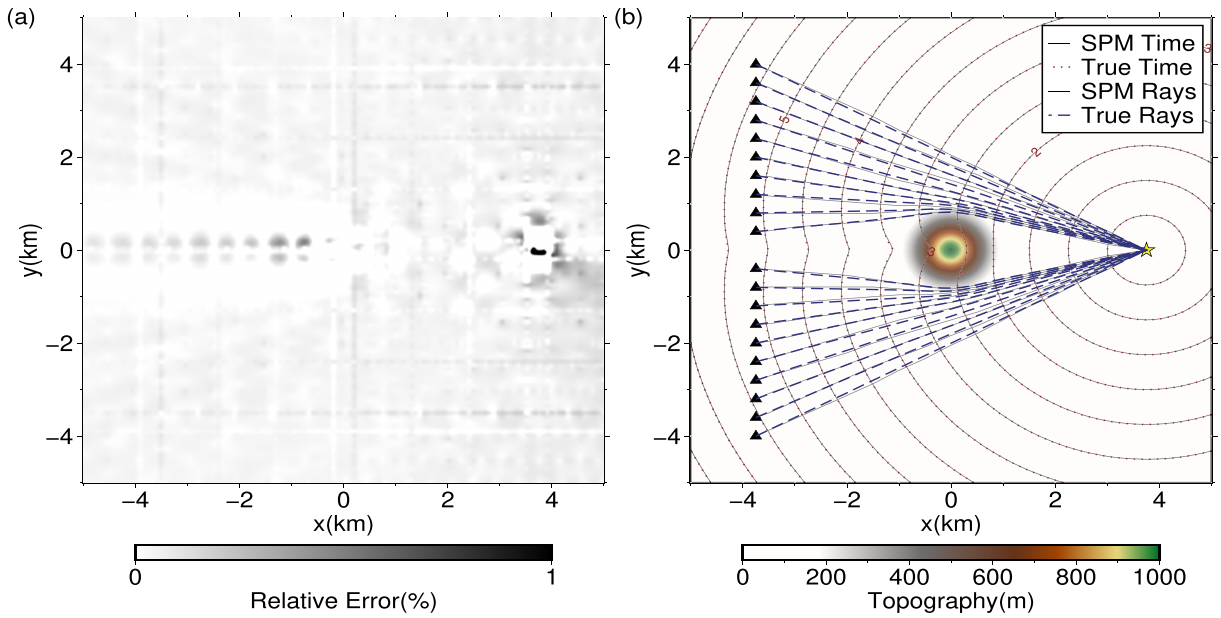

Figure 13. Same as Fig. 11, but the model comprises 20 elements in each direction, with 11 auxiliary nodes on each side.

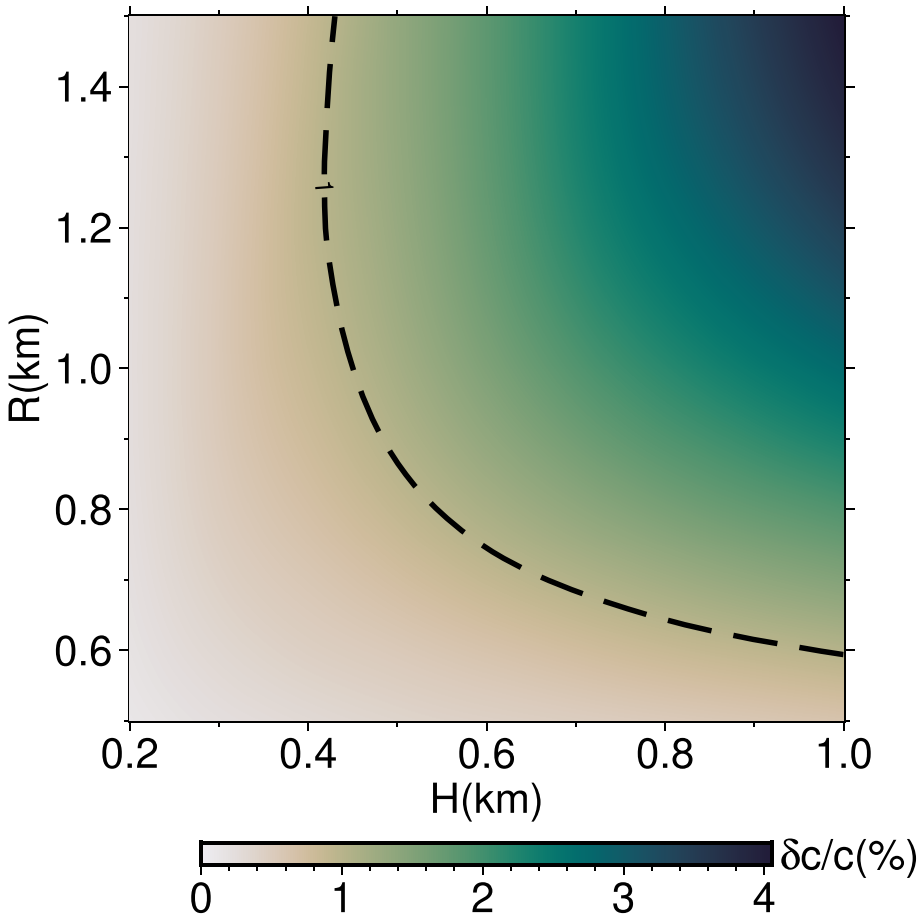

Figure 14. The $\delta c/c$ (in per cent, calculated by using eq. 25) for different (H, R) pairs. The black dashed line indicates the threshold value of 0.01.

the two models is a result of ray path length difference, ΔL, expressed as

$$\Delta t = t_{\text{topo}} - t = \frac{L_{\text{topo}} - L}{c} = \frac{\Delta L}{c}. \tag{23}$$

However, when topographic variations are not account for, this time difference will be mapped into variations in velocity as

$$\Delta t = \Delta\left(\frac{L}{c}\right) = -\frac{L\Delta c}{c^2}. \tag{24}$$

Here, the ray path length L (on the flat surface) is held constant as traveltime variations resulting from ray path variation are an order smaller than those from velocity perturbation based on the Fermat's principle. We can now assess the effect of not including topography in the ray tracing for phase/group velocity inversions by combining eqs (23) and (24) as

$$\frac{\Delta c}{c} = -\frac{\Delta L}{L}, \tag{25}$$

which suggest that we can ignore the effect of topography in the forward modelling process when the regional topography will not introduce ray path difference above a certain threshold (e.g. $|\Delta c/c| < 0.01$). However, it is important to note that computation of the ray path difference in eq. (25) involves curvature of the topographic surface and in most cases does not have closed-form geodesics. Here we propose a three-step analysis to determine whether topography can be neglected: First, we create an initial velocity model for the study region, and compute the phase velocity for a specific period. Then, for each typical source–station pair (in areas with strong topographic variation), we use SPM to compute the ray path length difference for the model with and without topography. Finally, we compute the average relative phase velocity variation for this region based upon eq. (25) and check whether it is below a given threshold.

We now show an example to examine how topographic parameters affect the relative dispersion velocity. To simplify the analysis, we define a Gaussian mountain as

$$z = H\mathrm{e}^{-(x^2+y^2)/R^2}, \tag{26}$$

where H refers to the maximum height of the mountain and R represents the horizontal radius. By systematically modifying H and R, we conducted a series of numerical experiments with the same source–station configuration as Fig. 2(b) to examine the corresponding changes in ray path variations for a fixed velocity of 1.5 km s^{-1}, as shown in Fig. 14. The black dashed line in the graph represents the threshold line, where $\Delta c/c = 0.01$. As expected, we observe that the relative velocity variation is affected by H and R jointly. In Supporting Information Section S2, we further investigate the topographic effects on the resulting 3-D models for two pairs of (H, R) selected from the regions with the relative phase velocity variation above and below the threshold.

6 CONCLUSION

We have proposed a new method to obtain 3-D shear wave velocity structures by including the topographic effects in surface wave tomography. In this method, we assume that surface waves propagate along the curved free surface of the Earth (i.e. topography) and traveltime can be modelled by the SPM with topography-adaptive mesh. Direct surface wave inversion is applied to invert 3-D shear wave velocity models from dispersion data by combining the automatically determined ray paths from SPM with surface wave 1-D Fréchet kernels. It is worth noting that our method is only suitable to capture the high-frequency propagation of surface wave, and the finite-frequency effects and diffraction phenomena arising from topography have been ignored.

Our new method has been successfully validated through synthetic tests and applied to real-data inversion, illustrating its potential in producing more accurate 3-D shear wave velocity structures. Our accuracy analysis shows that increasing the density of auxiliary nodes can enhance modelling accuracy. Our findings suggest that disregarding the topographic effect in surface wave inversion may result in ambiguous anomalies in the final images, particularly for regions with significant topographic variation. Furthermore, we have introduced a rule of thumb to quantify the impact of topographic effects on the 2-D phase/group velocity map.

ACKNOWLEDGMENTS

We would like to acknowledge Tongtong Xie for providing the surface wave dispersion curves of QCZ. We are grateful for the constructive feedback provided by Prof. Youshan Liu. DNQ wishes to thank Dr Bin He, Tianshi Liu and Ting Lei for their constructive suggestions. DNQ and QL are supported by the NSERC Discovery Grant (#487237). YTW and TX are supported by the Second Tibetan Plateau Scientific Expedition and Research Program (STEP; 2019QZKK0701), K. C. Wong Education Foundation (GJTD-2019-04), National Nature Science Foundation of China (42130807) and National Key Research and Development Program of China (2016YFC0600101). The figures presented in this work were created using the Generic Mapping Tools (Wessel *et al.* 2019).

DATA AVAILABILITY

The code for 2-D surface wave ray tracing and 3-D direct inversion is available on the GitHub page: https://github.com/nqdu/spmst. The data used in this study can also be found there.

SUPPORTING INFORMATION

Supplementary data are available at *GJI* online.

Figure S1. L-curve for the real-data inversion in Section 4. The best smoothing parameter is $\gamma = 4.08$.
Figure S2. NA inversion results for the average dispersion curve. Left: the model density and the best model. The red line is the inverted model through the average of the best 100 models. B-spline is utilized to obtain a 1-D smooth model. Right: observed (black line) and synthetic dispersion data (red line) from the inverted model. The grey zones around the data are the estimated uncertainties.
Figure S3. Inversion results on profile A–A′ for the Gaussian mountain checkerboard model with two H–R pairs. (a–c) Inversion results for $H = 500$ m and $R = 1$ km. (d–f) Inversion results for $H = 250$ m and $R = 1$ km. Panels (a) and (d) show inversion results with topography ignored. Panels (b) and (e) show inversion results with topography included. Panels (c) and (f) show the true model.

Please note: Oxford University Press is not responsible for the content or functionality of any supporting materials supplied by the authors. Any queries (other than missing material) should be directed to the corresponding author for the paper.

REFERENCES

Aki, K. & Richards, P.G., 2002. *Quantitative Seismology,* University Science Books.

Arroucau, P., Rawlinson, N. & Sambridge, M., 2010. New insight into Cainozoic sedimentary basins and Palaeozoic suture zones in southeast Australia from ambient noise surface wave tomography, *Geophys. Res. Lett.,* **37**(7), 256–265.

Aster, R.C., Borchers, B. & Thurber, C.H., 2018. *Parameter Estimation and Inverse Problems,* Elsevier.

Bai, C.-Y., Greenhalgh, S. & Zhou, B., 2007. 3D ray tracing using a modified shortest-path method, *Geophysics,* **72**(4), T27–T36.

Bai, C.-Y., Huang, G. & Zhao, R., 2010. 2-D/3-D irregular shortest-path ray tracing for multiple arrivals and its applications, *Geophys. J. Int.,* **183**(3), 1596–1612.

Barmin, M., Ritzwoller, M. & Levshin, A., 2001. A fast and reliable method for surface wave tomography, *Pure appl. Geophys.,* **158,** 1351–1375.

Bensen, G., Ritzwoller, M., Barmin, M., Levshin, A.L., Lin, F., Moschetti, M., Shapiro, N. & Yang, Y., 2007. Processing seismic ambient noise data to obtain reliable broad-band surface wave dispersion measurements, *Geophys. J. Int.,* **169**(3), 1239–1260.

Brocher, T.M., 2005. Empirical relations between elastic wavespeeds and density in the Earth's crust, *Bull. seism. Soc. Am.,* **95**(6), 2081–2092.

Cao, S. & Greenhalgh, S., 1993. Calculation of the seismic first-break time field and its ray path distribution using a minimum traveltime tree algorithm, *Geophys. J. Int.,* **114**(3), 593–600.

Chang, S.-J., Ferreira, A.M., Ritsema, J., van Heijst, H.J. & Woodhouse, J.H., 2015. Joint inversion for global isotropic and radially anisotropic mantle structure including crustal thickness perturbations, *J. geophys. Res.,* **120**(6), 4278–4300.

Chen, H., Zhu, L. & Su, Y., 2016. Low velocity crustal flow and crust–mantle coupling mechanism in Yunnan, SE Tibet, revealed by 3D S-wave velocity and azimuthal anisotropy, *Tectonophysics,* **685,** 8–20.

Dahlen, F. & Tromp, J., 1998. *Theoretical Global Seismology,* Princeton University Press.

Du, N., Li, Z., Hao, T., Xia, X., Shi, Y. & Xu, Y., 2021. Joint tomographic inversion of crustal structure beneath the eastern Tibetan Plateau with ambient noise and gravity data, *Geophys. J. Int.,* **227**(3), 1961–1979.

Fang, H., Yao, H., Zhang, H., Huang, Y.-C. & van der Hilst, R.D., 2015. Direct inversion of surface wave dispersion for three-dimensional shallow crustal structure based on ray tracing: methodology and application, *Geophys. J. Int.,* **201**(3), 1251–1263.

Gomberg, J.S. & Masters, T.G., 1988. Waveform modelling using locked-mode synthetic and differential seismograms: application to determination of the structure of Mexico, *Geophys. J. Int.,* **94**(2), 193–218.

Gruber, T. & Greenhalgh, S.A., 1998. Precision analysis of first-break times in grid models, *Geophysics,* **63**(3), 1062–1065.

Guo, Z., Wang, K., Yang, Y., Tang, Y., John Chen, Y. & Hung, S.-H., 2018. The origin and mantle dynamics of quaternary intraplate volcanism in Northeast China from joint inversion of surface wave and body wave, *J. geophys. Res.,* **123**(3), 2410–2425.

Hibert, C. *et al.*, 2014. Automated identification, location, and volume estimation of rockfalls at Piton de la Fournaise volcano, *J. geophys. Res.,* **119**(5), 1082–1105.

Jin, R., He, X., Fang, H., Xie, J., Liu, Y. & Zhang, P., 2023. Topography effect on ambient noise tomography: a case study for the Longmen Shan area, eastern Tibetan Plateau, *Geophys. J. Int.,* **233**(1), 1–12.

Köhler, A., Weidle, C. & Maupin, V., 2012. On the effect of topography on surface wave propagation in the ambient noise frequency range, *J. Seismol.,* **16,** 221–231.

Koulakov, I., Maksotova, G., Jaxybulatov, K., Kasatkina, E., Shapiro, N.M., Luehr, B.-G., El Khrepy, S. & Al-Arifi, N., 2016. Structure of magma reservoirs beneath Merapi and surrounding volcanic centers of Central Java modeled from ambient noise tomography, *Geochem. Geophys. Geosyst.,* **17**(10), 4195–4211.

Li, X.-W., Zhou, B., Bai, C.-Y. & Wu, J.-L., 2020. Seismic complex ray tracing in 2D/3D viscoelastic anisotropic media by a modified shortest-path method, *Geophysics,* **85**(6), T331–T342.

Lin, F.-C. & Ritzwoller, M.H., 2010. Empirically determined finite frequency sensitivity kernels for surface waves, *Geophys. J. Int.,* **182**(2), 923–932.

Miller, D.J., 2022. *Advances in Ambient Noise and Coda Wave Seismology at Hawaiian and Aleutian Arc Volcanoes,* The University of Wisconsin-Madison.

Moser, T., 1991. Shortest path calculation of seismic rays, *Geophysics,* **56**(1), 59–67.

Nunn, C., Roecker, S.W., Priestley, K.F., Liang, X. & Gilligan, A., 2014. Joint inversion of surface waves and teleseismic body waves across the Tibetan collision zone: the fate of subducted Indian lithosphere, *Geophys. J. Int.,* **198**(3), 1526–1542.

Paige, C.C. & Saunders, M.A., 1982. LSQR: an algorithm for sparse linear equations and sparse least squares, *ACM Trans. Math. Softw. (TOMS),* **8**(1), 43–71.

Rawlinson, N., Sambridge, M. & Saygin, E., 2008. A dynamic objective function technique for generating multiple solution models in seismic tomography, *Geophys. J. Int.,* **174**(1), 295–308.

Richter, C., 1943. Calculation of small distances, *Bull. seism. Soc. Am.,* **33**(4), 243–250.

Sambridge, M., 1999. Geophysical inversion with a neighbourhood algorithm–I. Searching a parameter space, *Geophys. J. Int.,* **138**(2), 479–494.

Saygin, E. & Kennett, B., 2012. Crustal structure of Australia from ambient seismic noise tomography, *J. geophys. Res.,* **117**(B1), B01304.

Schaeffer, A.J. & Lebedev, S., 2013. Global shear speed structure of the upper mantle and transition zone, *Geophys. J. Int.,* **194**(1), 417–449.

Schmandt, B. & Clayton, R.W., 2013. Analysis of teleseismic P waves with a 5200-station array in Long Beach, California: evidence for an abrupt boundary to Inner Borderland rifting, *J. geophys. Res.,* **118**(10), 5320–5338.

Schwab, F. & Knopoff, L., 1972. Fast surface wave and free mode computations, in *Methods in Computational Physics: Advances in Research and Applications,* vol. 11, pp. 87–180, Bolt, B. A., Elsevier.

Sethian, J.A. & Popovici, A.M., 1999. 3-D traveltime computation using the fast marching method, *Geophysics,* **64**(2), 516–523.

Shapiro, N.M., Campillo, M., Stehly, L. & Ritzwoller, M.H., 2005. High-resolution surface-wave tomography from ambient seismic noise, *Science,* **307**(5715), 1615–1618.

Shen, W. *et al.*, 2016. A seismic reference model for the crust and uppermost mantle beneath China from surface wave dispersion, *Geophys. J. Int.,* **206**(2), 954–979.

Shen, W. *et al.*, 2018. The crust and upper mantle structure of central and west Antarctica from Bayesian inversion of Rayleigh wave and receiver functions, *J. geophys. Res.,* **123**(9), 7824–7849.

Tromp, J., 1994. A coupled local-mode analysis of surface-wave propagation in a laterally heterogeneous waveguide, *Geophys. J. Int.,* **117**(1), 153–161.

Um, J. & Thurber, C., 1987. A fast algorithm for two-point seismic ray tracing, *Bull. seism. Soc. Am.,* **77**(3), 972–986.

Vidale, J., 1988. Finite-difference calculation of travel times, *Bull. seism. Soc. Am.,* **78**(6), 2062–2076.

Wang, K., Jiang, C., Yang, Y., Schulte-Pelkum, V. & Liu, Q., 2020. Crustal deformation in Southern California constrained by radial anisotropy from ambient noise adjoint tomography, *Geophys. Res. Lett.,* **47**(12), e2020GL088580.

Wang, S. & Sun, X., 2019. Topography effect on ambient noise tomography using a dense seismic array, *Earthq. Sci.,* **31**(5–6), 291–300.

Wang, Y., Lin, F.-C. & Ward, K.M., 2019. Ambient noise tomography across the Cascadia subduction zone using dense linear seismic arrays and double beamforming, *Geophys. J. Int.,* **217**(3), 1668–1680.

Wessel, P., Luis, J., Uieda, L., Scharroo, R., Wobbe, F., Smith, W.H. & Tian, D., 2019. The generic mapping tools version 6, *Geochem. Geophys. Geosyst.,* **20**(11), 5556–5564.

West, M., Gao, W. & Grand, S., 2004. A simple approach to the joint inversion of seismic body and surface waves applied to the southwest US, *Geophys. Res. Lett.,* **31**(15), L15615, doi: doi:10.1029/2004GL020373.

Woodhouse, J., 1974. Surface waves in a laterally varying layered structure, *Geophys. J. Int.,* **37**(3), 461–490.

Woodhouse, J. & Wong, Y., 1986. Amplitude, phase and path anomalies of mantle waves, *Geophys. J. Int.,* **87**(3), 753–773.

Xie, T., Xu, T., Ai, Y., Zeng, Q., Zhang, W. & Zheng, F., 2021. Imaging the shallow crustal velocity structure of the Qingchengzi ore field on the

Liaodong Peninsula, China, with a short-period dense array using ambient noise tomography, *Tectonophysics,* **813,** 228913.

Yang, Y., Ritzwoller, M.H., Levshin, A.L. & Shapiro, N.M., 2007. Ambient noise Rayleigh wave tomography across Europe, *Geophys. J. Int.,* **168**(1), 259–274.

Yomogida, K. & Aki, K., 1985. Waveform synthesis of surface waves in a laterally heterogeneous Earth by the Gaussian beam method, *J. geophys. Res.,* **90**(B9), 7665–7688.

Zeng, Q., Chen, R., Yang, J., Sun, G., Yu, B., Wang, Y. & Chen, P., 2019. The metallogenic characteristics and exploring ore potential of the gold deposits in eastern Liaoning Province, *Acta Petrol. Sin.,* **35**(7), 1939–1963.

Zhao, H., 2005. A fast sweeping method for eikonal equations, *Math. Comput.,* **74**(250), 603–627.

Zhou, B. & Greenhalgh, S., 2005. 'Shortest path' ray tracing for most general 2D/3D anisotropic media, *J. Geophys. Eng.,* **2**(1), 54–63.